

Magnetic and structural phase diagram of CaMn_2Sb_2 J. W. Simonson,^{1,*} G. J. Smith,¹ K. Post,² M. Pezzoli,^{1,3} J. J. Kistner-Morris,¹ D. E. McNally,¹ J. E. Hassinger,¹ C. S. Nelson,⁴ G. Kotliar,³ D. N. Basov,² and M. C. Aronson^{1,5}¹*Department of Physics and Astronomy, Stony Brook University, Stony Brook, New York 11794, USA*²*Department of Physics, University of California, San Diego, California 92093, USA*³*Department of Physics and Astronomy, Rutgers University, Piscataway, New Jersey 08854, USA*⁴*National Synchrotron Light Source, Brookhaven National Laboratory, Upton, New York 11793, USA*⁵*Condensed Matter Physics and Materials Science Department, Brookhaven National Laboratory, Upton, New York 11793, USA*

(Received 25 April 2012; published 29 November 2012)

On the basis of magnetic, transport, and optical measurements performed on single crystals, we report CaMn_2Sb_2 to be an antiferromagnetic insulator that exhibits weak ferromagnetic order above the Néel temperature. Magnetic susceptibility measurements reveal the magnitude of the high-temperature Curie-Weiss moment to be only half as large as the ground-state ordered moment, while electronic-structure calculations based on crystallographic measurements suggest a crystal-field-induced spin-state transition does not occur. The antiferromagnetic state is relatively insensitive to both doping and modest pressures, while the ferromagnetism can be readily tuned by either. Infrared transmission and pressure-dependent resistivity measurements suggest proximity to an electronic delocalization transition. We suggest the ferromagnetic state may be the signature of magnetic polarons.

DOI: [10.1103/PhysRevB.86.184430](https://doi.org/10.1103/PhysRevB.86.184430)

PACS number(s): 75.30.-m, 75.50.Ee, 72.20.-i, 78.20.-e

I. INTRODUCTION

The cuprate superconductors revealed that high-temperature superconductivity can arise near an electronic delocalization transition (EDT) from an antiferromagnetic insulating phase to a strongly correlated metal.¹ On the other hand, it has been put forth that the parent compounds of the superconducting Fe pnictides are situated just on the metallic side of a Mott-like EDT (Refs. 2,3), suggesting that superconductivity at higher temperatures may be realized if a new, insulating Fe-based parent compound could be synthesized. Despite the achievement of some degree of success to this end with the doped and pressurized Fe chalcogenide insulating phases $(\text{K,Tl})\text{Fe}_x\text{Se}_2$ (Refs. 4,5) and $R_2\text{O}_2\text{Fe}_2\text{O}(\text{Se}, \text{S})_2$ ($R = \text{La}, \text{Ce}, \text{Pr}, \text{Nd}, \text{Sm}$) (Ref. 6), superconducting critical temperatures T_c in this class of materials have yet to be significantly improved beyond the 55-K benchmark set in 2008.⁷

As a result of the inherent difficulty in enhancing the T_c 's of the Fe-based superconductors, some researchers have turned toward layered Mn pnictides. Virtually all such compounds are antiferromagnetic insulators and therefore make apt candidates to be potentially driven through EDTs by doping or pressure into a strongly correlated metallic state, the seedbed for unconventional superconductivity. Such efforts, however, had met with little success until recently. For example, both LaMnPO (Ref. 8) and BaMn_2As_2 (Ref. 9) were initially reported to remain insulators even when heavily doped. It is only now that we are beginning to uncover the means to metallize these compounds. LaMnPO has been reported to cross an EDT under the application of some 10 GPa,¹⁰ while LaMnAsO does so after Sr doping.¹¹ BaMn_2As_2 likewise metallizes with either the introduction of K as a dopant^{12,13} or the application of pressure.¹⁴ In none of these cases, however, has superconductivity yet been identified.

We became interested in the layered Mn pnictide CaMn_2Sb_2 after it was suggested to be close to a metal-insulator transition, albeit on the metallic side.¹⁵ As a result of that

ground-breaking study, CaMn_2Sb_2 became the subject of two neutron diffraction experiments, which determined the Néel temperature T_N to be 85–88 K and the static moment to lie between 2.8–3.4 μ_B/Mn ,^{16,17} although the magnetic models differ slightly with regard to the orientation of the moments. These studies revealed that when compared to the vast majority of layered Mn pnictides, CaMn_2Sb_2 is conspicuous for its relatively small static moment and its low ordering temperature, hundreds of degrees below those typical of such compounds. These qualities have been ascribed to the crystal structure of CaMn_2Sb_2 .¹⁶ Unlike BaMn_2Sb_2 , which forms in the more familiar ThCr_2Si_2 structure,¹⁸ CaMn_2Sb_2 takes the trigonal CaAl_2Si_2 structure type, which is characterized by corrugated triangular Mn layers. The crystallographic structure of CaMn_2Sb_2 is displayed in Fig. 1 along with that of BaMn_2Sb_2 for comparison.¹⁹ Although the nuclear structures appear similar at first glance, the Mn-Sb tetrahedra are rearranged in the Ca case, effectively buckling the Mn plane. As a consequence of this reorientation, the resulting magnetic structures and temperature scales of Mn-based CaAl_2Si_2 - and ThCr_2Si_2 -type compounds are strikingly different in general.

After learning that CaMn_2Sb_2 is singular in its metallic resistivity and low ordering temperature, we embarked upon a doping and pressure study in hopes that the attendant suppression of the magnetic state would give way to the first known Mn-based superconductor. In our initial measurements, however, we became aware that not only is CaMn_2Sb_2 an insulator, but the magnetic phase diagram is more complicated than had been realized. It has already been suggested that the magnetic measurements carried out in the original study were compromised by several trace magnetic impurities, and moreover, an 8% volumetric Sn impurity may have led to its original identification as a bad metal.¹⁶ Accordingly, we undertook an extensive investigation of the magnetic, transport, optical, and structural properties of this compound. Based on this investigation, we report that CaMn_2Sb_2 harbors

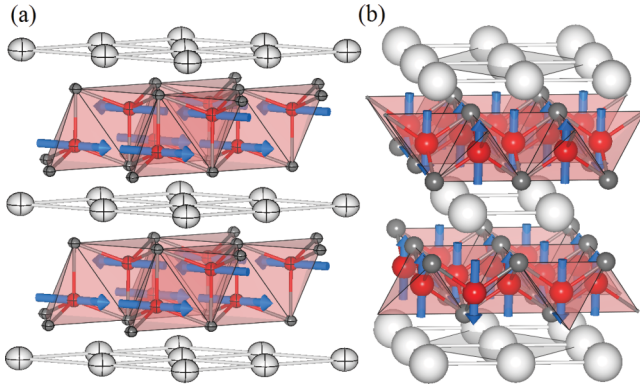


FIG. 1. (Color online) (a) The crystal structure of CaMn_2Sb_2 , which forms in the trigonal CaAl_2Si_2 structure type (S. G. $P\bar{3}m1$, no. 164). Ca atoms are shown in white, Mn atoms in red, and Sb atoms in gray. The Mn moments are indicated in blue (Ref. 16). (b) The familiar ThCr_2Si_2 -type structure of BaMn_2Sb_2 and its calculated magnetic structure, which is typical of Mn-based ThCr_2Si_2 -type compounds (Ref. 18). Ba atoms are drawn in white, and other colors are as in (a).

a ferromagnetic state above T_N and that a transition between large static and anomalously small fluctuating Mn moments occurs at T_N . We also detail the doping and pressure dependence of these results, which suggest proximity to an EDT.

II. EXPERIMENTAL PROCEDURE

We grew single crystals of CaMn_2Sb_2 as large as $5 \times 10 \times 3 \text{ mm}^3$ from a Sn flux, following a procedure similar to the established method,¹⁵ as well as from an In flux. Operations with Ca were carried out in an Ar-filled glove box to minimize oxidation. An initial composition of 2:4:4:15 Ca:Mn:Sb:Sn was found to result in the largest and highest-quality crystals. La doping was accomplished via the partial replacement of Ca with La and Na doping with NaCl via the cation exchange technique.²⁰ The crystals contained inclusions of Sn flux, but after treating the cleanest specimens with a 1% nital etchant solution, Meissner measurements of the corresponding superconducting volume fraction showed that we were able to produce crystals with between 0% and 3% Sn, a substantial improvement over the previous report. Polarized light microscopy measurements determined that the Sn inclusions, when present, were micron sized and distributed randomly through the crystal.

The $T = 300 \text{ K}$ structures and lattice parameters of both the doped and undoped crystals were verified using a Bruker Apex II Kappa diffractometer with Mo- $K\alpha$ radiation. The temperature dependencies of the lattice parameters were determined by four-circle high-resolution diffraction experiments carried out at beamline X21 of the National Synchrotron Light Source (NSLS) using an x-ray energy of 10 keV ($\lambda = 1.23985 \text{ \AA}$). The apparatus was aligned for triple-axis crystal geometry, and the primary and analyzing crystals were, respectively, Si(111) and LiF (200) aligned for the diffraction condition. The beam size was $1 \times 1 \text{ mm}^2$. The sample temperature was varied between 8 and 300 K via a closed-cycle refrigeration system. Magnetic measurements were carried out from 1.8 to 400 K in a Quantum Design Magnetic Properties Measurement System (MPMS), and an ac field

of 4.17 Oe was applied at 17 Hz for the ac susceptibility measurements. Resistivity measurements were performed with an ac current of $1 \mu\text{A}$ directed along the a axis in a Quantum Design Physical Properties Measurement System (PPMS). Such measurements performed under hydrostatic pressure were carried out in an EasyCell Pcell 30 in which a teflon cell was filled with a pressure-transmitting medium consisting of a 50-50 volumetric mixture of pentane and isopentane. The applied pressure was calibrated with manganin and Sn manometers. Because CaMn_2Sb_2 is an insulator, we have limited our measurements to the temperature range in which the voltage measurements remained Ohmic. Heat-capacity measurements were also performed in a PPMS from 1.8 to 300 K. Infrared (IR) transmission spectra were measured using a Bruker Vertex v/70 FT-IR spectrometer coupled to an IR microscope, which allowed us to obtain reliable data on small ($< 1 \text{ mm}^2$), thin (10–100 μm) crystals.

Electronic-structure calculations were carried out using the all-electron linearized augmented plane wave (LAPW) method as implemented in the WIEN2K code.²¹ We used the Perdew-Burke-Ernzerhof parametrization of the exchange-correlation potential in the generalized gradient approximation (GGA).²² The number of k points in the irreducible Brillouin zone was 192 and $R_{mt} \star K_{\text{max}} = 9.0$.

III. RESULTS

A. Basic properties of CaMn_2Sb_2

Figure 2 shows that CaMn_2Sb_2 is an insulator. In Fig. 2(a), we plot the temperature dependence of the ac electrical resistivity ρ , which increases by four orders of magnitude as the temperature is lowered from 300 to 8 K. A pronounced upturn is observed as the sample is cooled through $\sim 200 \text{ K}$ as well as a sharp decrease that coincides with $T_N = 85 \text{ K}$. The inset shows that at temperatures below and above this range, ρ is well described by activated behavior $\rho \propto \exp(\epsilon_{\text{act}}/2k_B T)$, where the transport gap ϵ_{act} is nearly the same in each region. We explain the discrepancy between our measurement and that of the previous study¹⁵ as the result of Sn inclusions in the latter's crystals that were introduced during flux growth. While diffraction measurements identified an 8% Sn contamination in samples produced by the original researchers,¹⁶ our Meissner effect measurements were unable to detect Sn in the crystal used to measure ρ . The original identification of CaMn_2Sb_2 as a bad metal was thus likely a result of electrical conduction through a percolating network of Sn inclusions, effectively shorting out the insulating bulk. This interpretation is consistent with the large ρ of the original sample, which is outside the range typical of bulk metals. Our measurement of crystals with vanishingly few Sn inclusions finds unambiguously that CaMn_2Sb_2 is an insulator.

Figure 2(b) displays the results of IR transmission measurements carried out on a single crystal of CaMn_2Sb_2 at 300 K, which confirm the presence of an optical gap at the Fermi level E_F . The crystal is transparent in the IR regime, but transmission decreases sharply above 8000 wave numbers, revealing an optical gap of $\epsilon_{\text{opt}} \approx 1.0 \text{ eV}$. The transmission is reduced below 3000 wave numbers, illustrating that states are present within this gap. It is possible that CaMn_2Sb_2 is

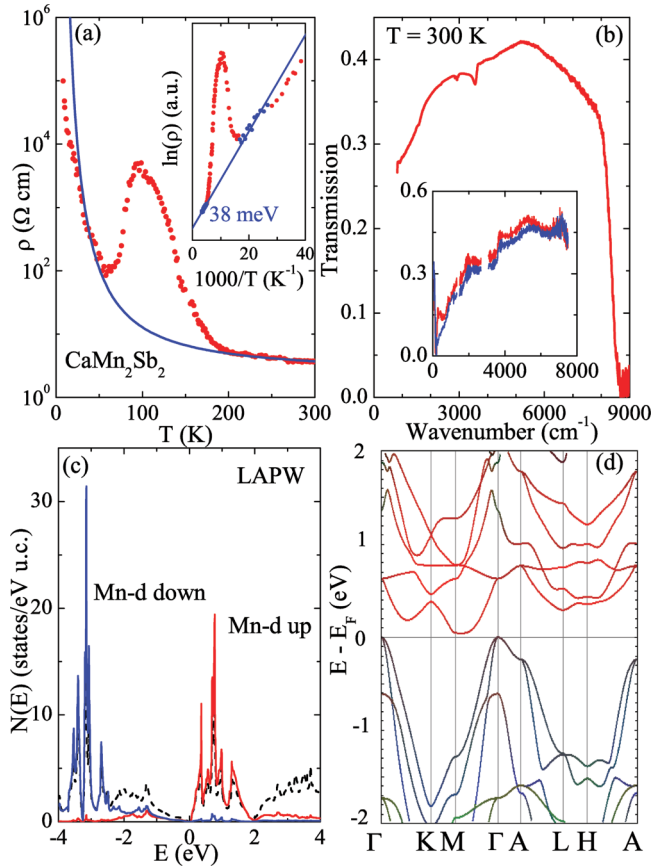


FIG. 2. (Color online) (a) The temperature dependence of the ac resistivity ρ of CaMn_2Sb_2 showing the increase as $T \rightarrow 0$ typical of an insulator. (b) Plot of infrared transmission as a function of wave number showing an optical gap of 1.0 eV and the presence of states within the gap below 3000 wave numbers. Inset: transmission measured at 35 K (blue curve) and 300 K (red curve). (c) Density of states $N(E)$ for antiferromagnetic CaMn_2Sb_2 . The projected $N(E)$ of Mn spin-up states is represented in red, the projected $N(E)$ of Mn spin-down states in blue, and the total $N(E)$ as a black dashed line. (d) The band structure for antiferromagnetic CaMn_2Sb_2 with Sb states shown in green and other colors as in (c).

close to an EDT in which these states would become the Fermi surface of an eventual metallic phase, but we must also consider the more conventional explanation that these states have an extrinsic origin. The lack of temperature dependence of the optical transmission shown in the inset to Fig. 2(b) suggests that phonon-assisted processes are not dominant in CaMn_2Sb_2 , and that excitations from the in-gap states to the extended states conserve momentum. This interpretation is further supported by the fact that ϵ_{opt} is significantly larger than ϵ_{act} , suggesting that E_F is pinned within these in-gap states.

In Figs. 2(c) and 2(d), we show the calculated spin-polarized density of states $N(E)$ and the electronic structure for CaMn_2Sb_2 , which nearly reproduce the observed direct gap at E_F and static magnetic moment as $T \rightarrow 0$ K. The calculation was performed assuming the antiferromagnetic structure determined by neutron diffraction measurements,¹⁷ taking atomic positions from x-ray diffraction measurements carried out at $\simeq 120$ K.¹⁵ As shown in Fig. 2(c), the bands near E_F primarily have Mn- d character with minor contributions

from Sb- p levels. The computed Mn moment is equal to $4 \mu_B/\text{Mn}$, somewhat larger than the values of 2.8 and $3.4 \mu_B/\text{Mn}$ reported by neutron diffraction experiments. The substantial (~ 4 eV) energy difference between spin-up and spin-down bands observed here appears to be a generic feature of this class of materials, as it has been reported for LaMnPO ,¹⁰ as well as BaMn_2As_2 and BaMn_2Sb_2 .²³ The electronic structure shown in Fig. 2(d) is similar to the one obtained by previous calculations,¹⁵ but we find that the occupied bands are shifted downward and the unoccupied bands upward so that an indirect gap of ~ 70 meV opens along the Γ - M direction. The direct gap of 0.6 eV at the center of the Brillouin zone that is found in our calculations is in good agreement with the measured $\epsilon_{\text{opt}} \approx 1.0$ eV. While the initial study employed the linear muffin-tin orbital method in its tight-binding representation with the atomic sphere approximation (TB-LMTO-ASA), we performed calculations with the LAPW method. The accuracy of the basis set of this method and its description of both the potential and the charge density without any spatial averaging allow us to resolve the gap, absent in the previous studies. Our calculation finds that CaMn_2Sb_2 is an insulator with both direct and indirect gaps, and the large magnetic moment obtained by the calculations suggests that the $3d$ electrons in CaMn_2Sb_2 are strongly correlated in the antiferromagnetic state.

Figure 3 displays the results of magnetic measurements on CaMn_2Sb_2 . We present zero-field ac susceptibility measurements with the ac field oriented along two crystallographic directions. The in-phase susceptibility χ' is shown in Fig. 3(a) and the out-of-phase component χ'' in Fig. 3(b). Above $\simeq 200$ K, χ' increases with decreasing temperature and shows no anisotropy when the ac field is aligned along the a and c axes, consistent with paramagnetic behavior. For temperatures between $\simeq 200$ and 85 K, there is a strong enhancement of χ' , particularly when the ac field is aligned with the a axis. The anisotropy in χ' within this range is displayed in the inset to Fig. 3(b) and reaches a value of 1.6. The ac susceptibility χ' is strongly reduced and becomes almost isotropic with the onset of antiferromagnetic order at 85 K. The magnitude of the peak in χ' is halved with the application of a dc field of 50 Oe and nearly completely suppressed with only 500 Oe, which together with our improved sample quality explains their absence from previous studies. The temperature dependence of the imaginary part of the ac susceptibility χ'' indicates that there are two distinct phase transitions, the familiar antiferromagnetic order at 85 K, and a new transition at 210 K, where sharp peaks in χ'' are observed [Fig. 3(b)]. The strong enhancement of χ' for temperatures between 85 and 210 K and its rapid suppression by magnetic field suggest that CaMn_2Sb_2 becomes ferromagnetic near 200 K.

We performed an Arrott plot analysis to confirm the existence of ferromagnetic order below $\simeq 210$ K, and the results are shown in Figs. 3(c) and 3(d). Figure 3(c) shows the magnetic isotherms collected from 1.8 to 400 K. We subtracted a linear paramagnetic contribution from each isotherm before proceeding with further analysis. The Arrott plot analysis is presented in Fig. 3(d). The magnetic isotherms are observed to become linear at high fields, with the $T_C = 210$ K isotherm giving $M^2 = 0$ when extrapolated to $H/M = 0$. These measurements show that CaMn_2Sb_2

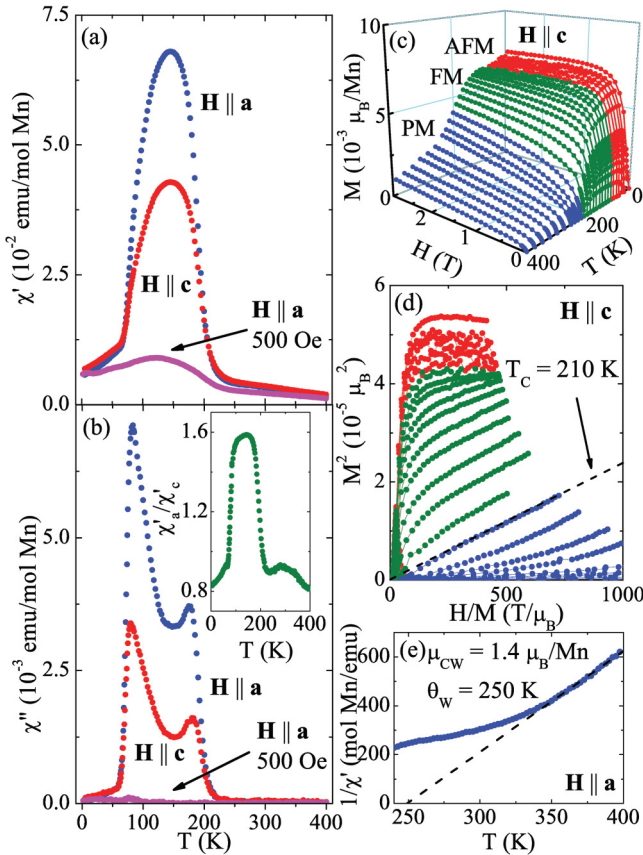


FIG. 3. (Color online) (a) The temperature dependence of the in-phase part of the zero-field ac susceptibility χ' of CaMn_2Sb_2 showing enhancement between $T_N = 85$ K and $T_C = 210$ K. Data that were taken with the field \mathbf{H} parallel to the a axis are shown in blue and parallel to the c axis are shown in red. The magenta curve shows the effect of a 500-Oe dc field on the ac susceptibility. (b) The temperature dependence of the out-of-phase part of the zero-field ac susceptibility χ'' with colors as in (a). χ'' exhibits sharp peaks at both transitions. Inset: the ratio of χ' with $\mathbf{H}\parallel a$ and with $\mathbf{H}\parallel c$ as a function of temperature. (c) Magnetization M measured as a function of dc H at different temperatures in the antiferromagnetic (red), ferromagnetic (green), and paramagnetic (blue) states. A linear paramagnetic contribution has been subtracted for clarity. (d) Arrott plot analysis of CaMn_2Sb_2 where the critical isotherm is shown to occur at $T_C = 210$ K. Colors are as in (c). The dashed line through the critical isotherm is a linear extrapolation of the high-field magnetization to $H = 0$. (e) The temperature dependence of $1/\chi'$ in the paramagnetic state. The dashed line is a fit to the Curie-Weiss law corresponding to a fluctuating moment of $\mu_{\text{CW}} = 1.4 \mu_B/\text{Mn}$ and Weiss temperature $\theta_w = 250$ K.

becomes ferromagnetic below 210 K, albeit with a very small spontaneous moment of $7.3 \times 10^{-3} \mu_B/\text{Mn}$, too small to be detected by neutron diffraction measurements. The magnetization isotherms in Fig. 3(c) are suggestive that the ferromagnetic moment persists into the antiferromagnetic phase, implying that it might better be described as a canted antiferromagnet. It would be interesting to revisit the neutron diffraction measurements to see if the data support this conclusion.

Figure 3(e) shows that the paramagnetic state of CaMn_2Sb_2 is local-moment-like, obeying the Curie-Weiss relation for

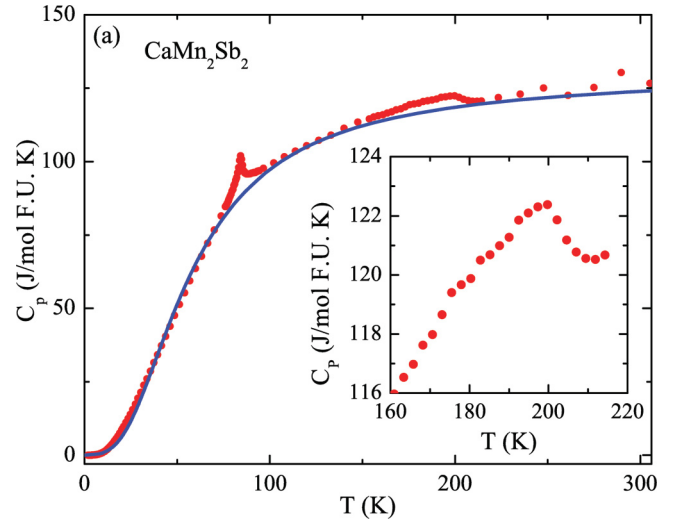


FIG. 4. (Color online) (a) The temperature dependence of the heat capacity C_p of CaMn_2Sb_2 shows a sharp peak at $T_N = 85$ K and a broad peak with onset at $T_C = 210$ K. The phonon contribution C_{phonon} obtained from Debye's law is given by the blue solid line. Inset: closer look at the peak associated with the onset of ferromagnetic order.

$T \gtrsim 340$ K when $1/\chi'$ is plotted against temperature with the field parallel to the a axis. The Weiss temperature $\theta_w = 250$ K is positive, indicating that the prevailing local-moment fluctuations are ferromagnetic in character. That $\theta_w \approx T_C$ implies that CaMn_2Sb_2 is subject to minimal effects from frustration or low dimensionality. Most interestingly, the fluctuating moment corresponds to only $1.4 \mu_B/\text{Mn}$, less than half the ordered moment seen in the antiferromagnetic ground state.^{16,17} This observation hints at the occurrence of a significant modification to the electronic structure between T_N and the high-temperature paramagnetic state. It is unclear from these data, however, whether this transition is the result of a restructuring of the energetic hierarchy of the Mn-3d atomic orbitals or whether enhanced hybridization due to Mn-3d Sb-5p orbital overlap occurs with the advent of the high-temperature phase. In either case, we expect crystallographic measurements to provide further details.

Both the antiferromagnetic and ferromagnetic transitions are also visible in the heat-capacity C_p measurements shown in Fig. 4. The Debye expression

$$C_p \approx 9Nk(T/\Theta) \int_0^{\Theta/T} dx e^x x^4 / (e^x - 1)^2 \quad (1)$$

was used to estimate the phonon contribution to $C_p(T)$, yielding a characteristic temperature of $\Theta = 234$ K. The antiferromagnetic transition is marked by a lambda-type peak at 85 K, whereas the ferromagnetic transition occurs with a broader peak, clearly seen in the inset to Fig. 4. This measurement suggests that the ferromagnetic transition is bulk in nature, despite its small moment. These results provide yet further confirmation of the existence of two separate magnetic transitions, which we observed in electrical resistivity, magnetic susceptibility, and now in heat-capacity measurements.

Figure 5 presents the results of our high-resolution x-ray diffraction measurements, which reveal a continuous

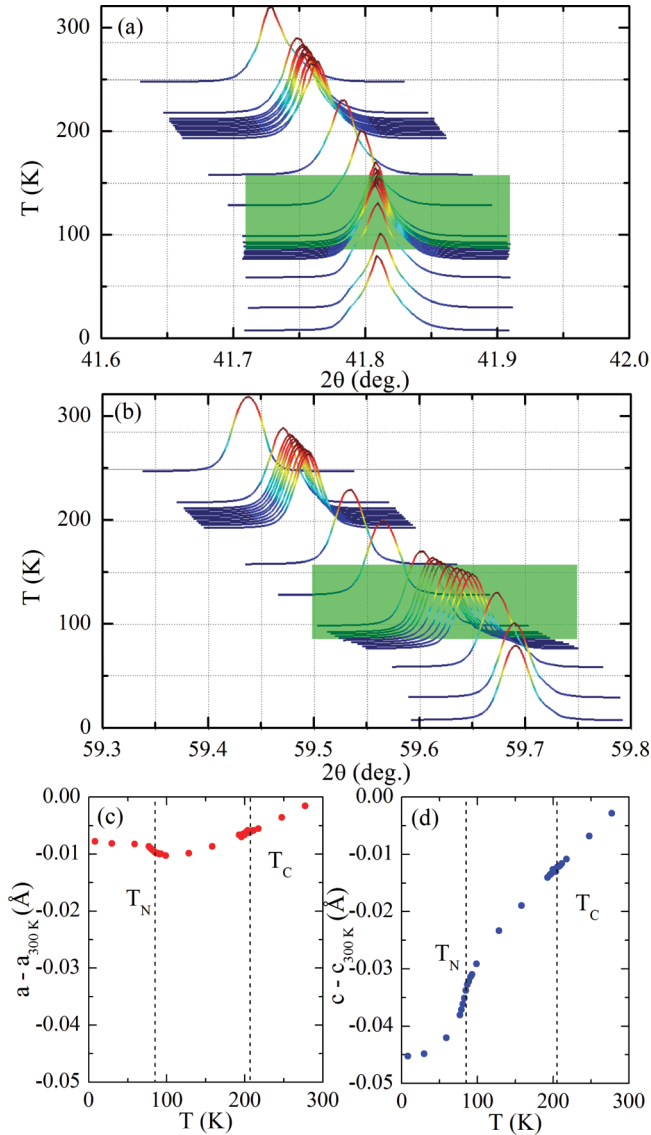


FIG. 5. (Color online) (a) An overlay of x-ray diffraction patterns of the $(\bar{2}02)$ peaks of CaMn_2Sb_2 at several different temperatures showing the linear change in position at temperatures above T_N (green translucent plane) and the constant position below. (b) As (a) but with the $(\bar{1}\bar{1}5)$ instead, showing its rapid change in position at temperatures near T_N . (c) The temperature dependence of relative changes in the a lattice parameter (red) as determined from the position of the peaks in (a) and (b). Error bars are smaller than the size of the colored circles. (d) A plot of the temperature dependence of relative changes in the c parameter (blue) on an identical scale to the plot in part (c), which shows its length to decrease rapidly near T_N . Again, error bars are smaller than the size of the colored circles.

compression of the c lattice parameter and accompanying increase in the a parameter just as CaMn_2Sb_2 enters the antiferromagnetic state. Figure 5(a) shows the temperature dependence of the $(\bar{2}02)$ peak, the position of which is predominantly determined by the length of the shorter a parameter. The angular position of this peak increases nearly linearly as the temperature is lowered from 300 to 100 K. By 91 ± 3 K, however, the continuous shift of this peak with temperature abates, and its angular position remains constant to tempera-

tures as low as 8 K, indicating that further a -axis contraction is halted at the onset of the antiferromagnetic state. Notably, the change in the $(\bar{2}02)$ peak position with temperature does not display any departure from linearity near $T_C = 210$ K, indicating that the appearance of the ferromagnetic state has minimal effect on the underlying crystallographic structure. Figure 5(b) shows the data from the $(\bar{1}\bar{1}5)$ peak, the relative position of which is dominated by changes in the c parameter. Again, the temperature dependence of the peak is nearly linear between 300 and 100 K with no marked divergence at T_C . The peak position shifts sharply by 0.05° between 77 and 98 K, however, indicating a corresponding reduction in the c lattice constant across the same temperature range.

The implications of these results are apparent in the temperature dependencies of the a and c lattice parameters, the relative changes of which are plotted on identical scales in Figs. 5(c) and 5(d). Above T_N , both parameters decrease linearly as the temperature is lowered from 300 K, displaying no signature at T_C . Near T_N , the a parameter displays a 0.03% increase upon ordering and then remains constant as the temperature is reduced as low as 8 K. Meanwhile, contraction in the c parameter accelerates near T_N , decreasing by approximately 0.14% within the range $T_N \pm 10$ K. These results suggest that the modification to the electronic structure inferred from the discrepancy between ordered and fluctuating moments occurs at T_N and not T_C . Regardless, the unit-cell parameters indicate that the crystal symmetry remains in the hexagonal crystal family both above and below this transition, even if we can not comment on a modification to the set of symmetry operators.

B. La- and Na-doped CaMn_2Sb_2

In the course of this work, we have arrived at a new understanding of CaMn_2Sb_2 as a correlated insulator, similar to the related Mn pnictide compounds LaMnPO and BaMn_2As_2 . CaMn_2Sb_2 , however, differs from these compounds in several key ways, including its low ordering temperature, the observation of gap states in the IR spectra, an anomalously small degree of local magnetic character in the paramagnetic phase, and a weak ferromagnetic phase. Do these characteristics signify that CaMn_2Sb_2 is closer to an EDT than other Mn pnictides? The results of doping and pressure studies aimed at answering this question are presented here.

Doping flux-grown crystals presents some uncertainty regarding the actual dopant concentration that is achieved by the conclusion of the growth process. In general, a portion of the dopant species may remain dissolved in the liquid flux even after crystal growth is complete. Accordingly, we have taken steps to quantify the La and Na concentrations present within doped CaMn_2Sb_2 . Summarized in Table I are the results of

TABLE I. Measured compositions of crystals grown from fluxes with different dopant to Ca ratios.

Dopant:Ca ratio in flux	Dopant percentage of Ca site
1 La : 9 Ca	3.7(1)%
1 La : 4 Ca	5.1(1)%
1 Na : 9 Ca	0.54(2)%
1 Na : 4 Na	0.83(1)%

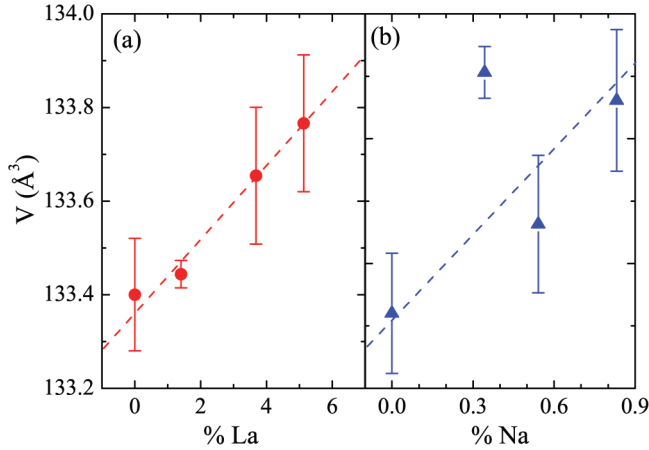


FIG. 6. (Color online) (a) The cell volume of La-doped CaMn_2Sb_2 as a function of La concentration. (b) The cell volume of Na-doped CaMn_2Sb_2 as a function of Na concentration. The dashed lines are guides for the eye.

direct-current plasma optical emission spectrometry (DCP-OES) measurements carried out on the doped crystals (ATI Wah Chang, Albany, Oregon). These measurements reveal that substantial levels of each dopant species must be present during the flux growth process in order to obtain even relatively low concentrations in the doped crystals. Compositions given in this paper reflect the measured values listed in the table. Moreover, we note a Vegard's-rule-like dependence of the lattice on the measured dopant concentration. As shown in Fig. 6, both dopants increase the volume of the unit cell at a linear rate. These observations independently verify that both La and Na have been successfully doped into the crystals.

As shown in Figs. 7(a)–7(c), doping CaMn_2Sb_2 with La monotonically decreases χ , while Na doping increases χ . The temperature dependencies of χ' and χ'' of the doped compounds are presented in Figs. 7(a) and 7(b). Basic charge counting suggests that replacing 5% of the Ca site with La^{3+} ions would correspond to electron doping, while Na^{1+} doping would correspond to hole doping. We note that both dopants increase the unit-cell volume, suggesting that chemical pressure has a secondary effect. With La doping, the peaks in χ'' at T_N and T_C are diminished, but neither transition temperature is modified. Na doping, on the other hand, has the opposite effect; χ' is enhanced by an order of magnitude in the antiferromagnetic and paramagnetic states when only 0.8% Na is instead doped on the Ca site. What is more, the plateaulike feature associated with ferromagnetism shifts to higher temperatures, suggesting that $\text{Na}_{0.008}\text{Ca}_{0.992}\text{Mn}_2\text{Sb}_2$ is ferromagnetic between 170 and 270 K. The same shift is borne out in the χ'' data, which feature peaks at both 170 and 270 K. As can be seen in Fig. 7(c), a small peak remains in χ' at 85 K, suggesting that T_N has not changed. These results reveal systematic changes in the magnitude of χ with doping. Only Na doping has any significant effect on the transition temperatures, however, and in neither case is T_N substantially reduced.

Heat-capacity measurements performed on $\text{Ca}_{0.95}\text{La}_{0.05}\text{Mn}_2\text{Sb}_2$ are in agreement with the susceptibility, as displayed in Fig. 7(d). Even with 5% La doping, the transition at T_N is shifted only 2 K to 83 K. Meanwhile, the signature of

the transition in the heat capacity is broadened from a width of about 4 K in the undoped case to about 6 K. These data indicate that significant suppression of T_N does not occur with La doping, just as Fig. 7(c) showed for $\text{Na}_{0.008}\text{Ca}_{0.992}\text{Mn}_2\text{Sb}_2$.

Figure 7(e) shows that CaMn_2Sb_2 remains insulating even when doped with La or Na. Even if Na doping reduces ρ by two orders of magnitude, ρ nonetheless increases sharply as the temperature is lowered, particularly for $T < 20$ K. A rapid decrease occurs at T_N , similar to our observation of CaMn_2Sb_2 . Taken with the peak in χ' shown in Fig. 7(c), this feature confirms that T_N is nearly unaffected by Na doping. Electron doping with La, however, actually increases ρ . As seen in the figure, this effect rapidly increases as the temperature is lowered, with greater La concentration resulting in even larger ρ . The downturn typically observed upon reaching T_N is absent in the La-doped samples, even if its signature remains in the χ' , χ'' , and heat-capacity measurements. With Na doping, the observation of enhanced conductivity, lack of metallization, and minimal change in T_N are reminiscent of our previous report of F-doped LaMnPO .⁸ The enhanced resistivity of La-doped CaMn_2Sb_2 , however, represents an anomalous effect previously unreported to our knowledge, at least in the case of Mn pnictides.

The IR transmission measurements displayed in Fig. 7(f) are consistent with these ρ measurements, confirming that the doped crystals remain insulating. With Na doping, the transmission is systematically reduced across the entire infrared spectrum. The sharp decrease near 8000 wave numbers indicates that the optical gap of ~ 1 eV is virtually unaffected. Meanwhile, the presence of states within the gap remains clear at the low wave numbers. Transmission through the La-doped samples, however, indicates a sharp reduction in the size of the gap, with the drop in transmission now only occurring at 2000 wave numbers, indicating an optical gap of only ~ 0.25 eV. Notably, the transmission at low wave number is indeed higher with La doping,²⁴ thanks to the presence of states located within the gap of the undoped compound, in agreement with the heightened ρ in this compound.

Figure 7(g) shows that the rapid c parameter contraction measured in CaMn_2Sb_2 is not observed in the 0.8% Na-doped crystal: both the a and c lattice parameters decrease smoothly across T_N . We note that our x-ray diffraction measurements confirm that the crystal structure at $T = 300$ K remains unchanged for either dopant, aside from a small increase to the a and c lattice parameters in either case. For Na-doped CaMn_2Sb_2 , the only mark of magnetic order is a gradual reduction in lattice compression within the antiferromagnetic state. Further, no feature corresponds to T_C or to the purported low-temperature boundary of the ferromagnetic state T_f . Moreover, while the c parameter of undoped CaMn_2Sb_2 decreases seven times as much as the a constant across the entire temperature range, the relative decreases in $\text{Na}_{0.008}\text{Ca}_{0.992}\text{Mn}_2\text{Sb}_2$ fall within a factor of 2 of one another. Taken together, these observations reveal strikingly different magnetoelasticities in these two materials, despite their minimal difference in T_N . It is likely given these results that the reduction of the fluctuating moment observed in the paramagnetic state of the undoped compound is quite sensitive to chemical concentration and may very well be completely absent in the Na-doped compound. Because the ferromagnetic state occurs at a higher temperature

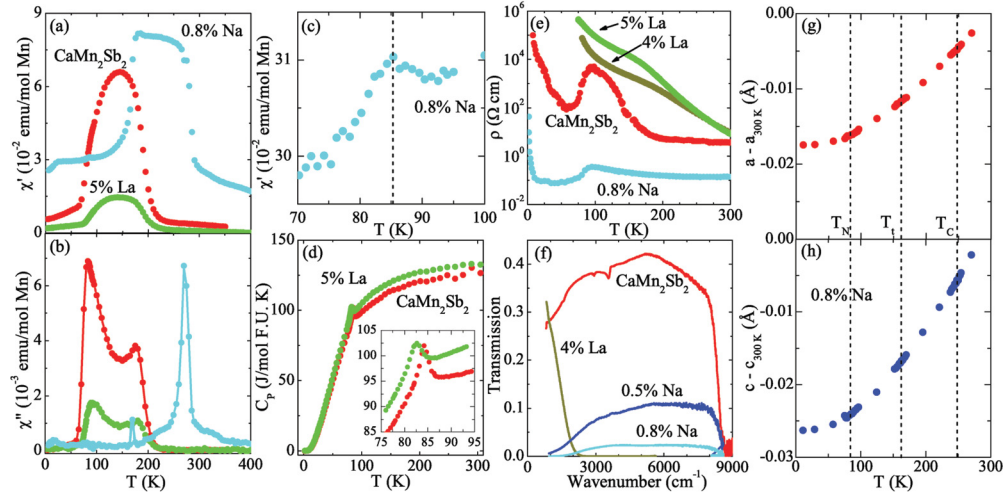


FIG. 7. (Color online) (a) The temperature dependence of χ' of CaMn_2Sb_2 (red curve), $\text{Na}_{0.008}\text{Ca}_{0.992}\text{Mn}_2\text{Sb}_2$ (blue curve), and $\text{Ca}_{0.95}\text{La}_{0.05}\text{Mn}_2\text{Sb}_2$ (green curve) showing enhancement with Na doping and decrease with La doping. (b) The temperature dependence of χ'' with the same colors as in (a) showing peaks at magnetic transitions. (c) The temperature dependence of χ' of $\text{Na}_{0.008}\text{Ca}_{0.992}\text{Mn}_2\text{Sb}_2$ near $T_N = 85$ K showing that T_N is unchanged with Na doping. (d) The heat capacity of CaMn_2Sb_2 and $\text{Ca}_{0.95}\text{La}_{0.05}\text{Mn}_2\text{Sb}_2$ [colors as in (a)] showing minimal decrease in T_N with La doping. (e) The temperature dependence of ρ of CaMn_2Sb_2 , $\text{Na}_{0.008}\text{Ca}_{0.992}\text{Mn}_2\text{Sb}_2$, $\text{Ca}_{0.95}\text{La}_{0.05}\text{Mn}_2\text{Sb}_2$, and $\text{Ca}_{0.96}\text{La}_{0.04}\text{Mn}_2\text{Sb}_2$ [yellow curve, others as in (a)] to show decrease with Na doping and increase with La doping. (f) IR transmission spectra of CaMn_2Sb_2 , $\text{Na}_{0.008}\text{Ca}_{0.992}\text{Mn}_2\text{Sb}_2$, $\text{Ca}_{0.96}\text{La}_{0.04}\text{Mn}_2\text{Sb}_2$, and $\text{Na}_{0.005}\text{Ca}_{0.995}\text{Mn}_2\text{Sb}_2$ [dark blue curve, others as in (e)]. Transmission is reduced with Na doping, while the gap itself is reduced with La doping even if low wave-number transmission is enhanced. (g), (h) The temperature dependence of the a (red curve) and c (blue curve) lattice parameters of $\text{Na}_{0.008}\text{Ca}_{0.992}\text{Mn}_2\text{Sb}_2$ determined from the position of the (213) and (103) peaks. Error bars are smaller than the size of the colored circles.

with Na doping relative to undoped CaMn_2Sb_2 , however, the decomposition of the crystals at temperatures approaching 500 K precludes a direct measurement of this quantity.

C. High-pressure ρ measurements

Given the limited success in reducing T_N or achieving a metallic state with doping, we proceeded to evaluate pressure as a tuning parameter. The pressure-dependent ρ measurements presented in Fig. 8(a) reveal that the ferromagnetic state is rapidly suppressed with only small pressures. Measurements of ρ at temperatures below 10–30 K were not possible due to the insulating nature of CaMn_2Sb_2 . Although the data measured at 1 bar feature a sharp upturn as the sample is cooled below $T_C = 200$ K, this feature is restricted to temperatures below 120 K with only 0.3 GPa and completely extinguished by 1.4 GPa. Interestingly, ρ at $T = 300$ K actually increases with pressure until 1.2 GPa, the highest pressure measured before the complete suppression of the ferromagnetic state, whereupon it begins to decrease with further pressure. CaMn_2Sb_2 remains an insulator at the highest pressure investigated, 1.6 GPa, and indeed ρ at this pressure is higher than at ambient pressure at both 300 and 30 K. A sharp drop in ρ upon reaching antiferromagnetic order is present at all pressures measured, from which we observe that T_N decreases by 7 K from its ambient pressure value of 85 K with the application of 1.6 GPa. The pressure dependence of T_N and T_C is shown in Fig. 8(b). Naïvely extrapolating T_N to zero, we estimate complete suppression of the antiferromagnetic state by ~ 20 GPa. Overall, these results speak to the strong pressure dependence of the ferromagnetic state and the moderate pressure dependence of the antiferromagnetic state.

IV. DISCUSSION

Our study of high-quality single crystals of both pure and La- and Na-doped CaMn_2Sb_2 has revealed three primary results: that a ferromagnetic state persists above T_N ; that the fluctuating moment in the high-temperature paramagnetic state is anomalously small; and that CaMn_2Sb_2 may be near an EDT. We will discuss each of these results in turn.

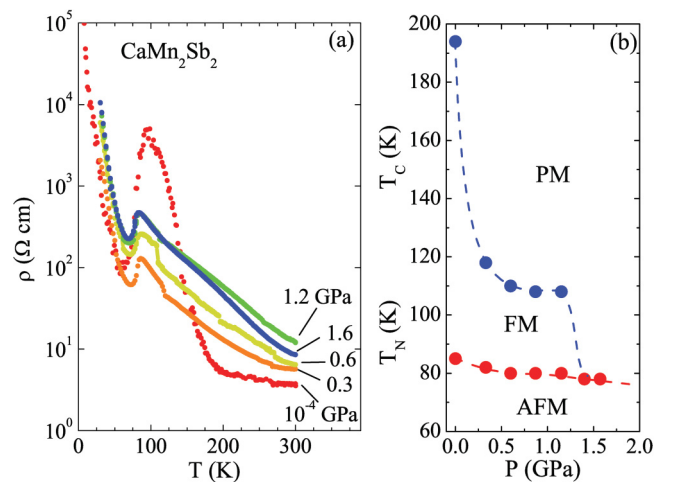


FIG. 8. (Color online) (a) The temperature dependence of ρ of a CaMn_2Sb_2 single crystal measured at several different pressures: 1 bar (red curve), 0.3 GPa (orange curve), 0.6 GPa (yellow curve), 1.2 GPa (green curve), 1.6 GPa (blue curve). The feature associated with the ferromagnetic state is rapidly and continuously suppressed. (b) T_N (red curve) and T_C (blue curve) as extracted from the resistivity data are plotted as a function of pressure.

Because CaMn_2Sb_2 is an insulator, the Mn moments must remain spatially localized, and the occupation of the d orbitals should lead to ordered moments as large as $\simeq 5 \mu_B/\text{Mn}$ in the high-spin configuration, to just $1\text{--}2 \mu_B/\text{Mn}$ when the crystal-field splitting is weak relative to the exchange. Thus, the observation of ferromagnetic order with a moment of only $7.3 \times 10^{-3} \mu_B/\text{Mn}$ is intriguing. Ferromagnetic contamination is an obvious concern, but there are a number of reasons why this is an unlikely explanation in our crystals. First, the anisotropy in the susceptibility is consistent with the trigonal symmetry of the underlying crystal, which would be unexpected for contaminant inclusions. What is more, the 100-fold increase in resistance that coincides with the susceptibility peak is also much too large to be explained by the presence of an inclusion whose conducting state is affected by the onset of ferromagnetic order since an inclusion that has a resistivity much larger than the CaMn_2Sb_2 host would carry no current. Finally, the magnitude of the specific-heat anomalies at the ferromagnetic and antiferromagnetic transitions are similar, suggesting that both are bulk phenomena. For all these reasons, it is likely that the weak ferromagnetism in CaMn_2Sb_2 is intrinsic.

The magnetization and transport data are suggestive that this weak ferromagnetism stems from the formation of magnetic polarons, such as those reported in Eu-based compounds,²⁵ manganites,²⁶ and more recently in superconducting Se-doped FeTe.²⁷ Magnetic polarons originate in magnetic insulators when electrons are spatially localized via the Coulomb potential at states within the band gap. The spins of these bound states are exchange coupled to those of nearby Mn atoms, yielding a region where host moments have aligned ferromagnetically. Only electrons near E_F participate in this process, resulting in a small moment, but they can have a very large effect on the electrical resistivity as the charge carriers become bound. In striking agreement with our own measurements on CaMn_2Sb_2 , peaks in ρ of up to four orders of magnitude above the activated behavior have been reported in EuSe,²⁸ where the peak drops back to the activated line with the onset of antiferromagnetic order.

We may qualitatively explain the observed resistivity of CaMn_2Sb_2 according to this model. Above T_C , the polarons have not yet formed, allowing the charge carriers to conduct freely. Resistivity increases sharply below this temperature, and polarons form as the average kinetic energy of the electrons decreases, leading to the observed onset of ferromagnetism in measurements of χ . Below T_N , we hypothesize that strong antiferromagnetic exchange imposes a rearrangement from the locally coaligned ferromagnetic spins of nearest-neighbor Mn atoms in favor of the long-range antiferromagnetic order observed in neutron experiments. As the charge carriers thereby decouple from the lattice, they are no longer bound, and resistivity drops back to the typical activated behavior expected of an insulator.

These anomalous features vary consistently among crystals grown in different batches. The ferromagnetic moment is always on the order of $10^{-3} \mu_B/\text{Mn}$, but there are variations within this regime, as displayed in Fig. 9(a). Figure 9(b) shows that crystals with large moments also exhibit stronger susceptibilities in the ordered state, while the small moment samples have distinctly lower T_C 's. What is more, Fig. 9(c) shows that the enhanced resistivity is likewise related to the

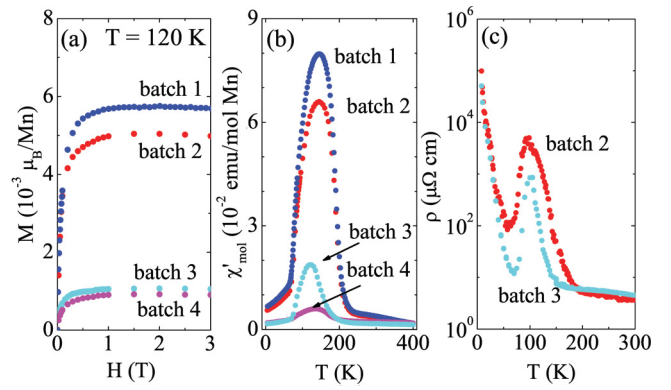


FIG. 9. (Color online) (a) M at $T = 120$ K of four different crystals as a function of dc H . (b) Temperature dependence of χ' for the same crystals shown in (a) exhibiting different magnitude and apparent T_C , colors as in (a). (c) Temperature dependence of ρ of two crystals from same batches as those in (a), colors also as in (a).

size of the moment, while the activated contribution is nearly sample independent. The same reduction in T_C is also observed in ρ measurements, indicating that the ferromagnetism does not stem from an extrinsic phase, for which T_C would be constant. Consistent with these results, magnetic polarons have been found to be prone to formation near atomic site defects,²⁹ the concentration of which may vary from sample to sample. We suggest that a finite but variable number of electrons in each CaMn_2Sb_2 crystal are collectively bound at T_C , coaligning with \mathbf{H} to generate the observed moment while proportionally draining charge carriers from the system.

Like virtually all layered Mn pnictides,³⁰ the ground state of CaMn_2Sb_2 is antiferromagnetic and insulating with each Mn atom possessing a substantial moment. Even so, measurements of χ in the paramagnetic regime reveal a fluctuating moment only half as large per magnetic atom as observed in the ground state. Given the history of atomic spin-state transitions in Mn pnictides (most notably MnAs),³¹ we originally considered this observation to be a manifestation of a transition between a so-called high-spin ground state and a low-spin paramagnetic state. In MnAs, antiferromagnetic order prevails below $T_N = 49$ K but gives way to ferromagnetism until $T_C = 313$ K, whereupon the compound undergoes a first-order phase change from a hexagonal structure to a low-spin paramagnet with a distorted orthorhombic structure and a moment of $2\text{--}3 \mu_B/\text{Mn}$. At $T_1 = 398$ K, it undergoes a second-order phase change back to the same hexagonal structure and to high-spin Curie-Weiss-type paramagnetism with a moment of $4.95 \mu_B/\text{Mn}$.^{32,33} In general, so-called high-spin/low-spin transitions result from the competition between the energy scales of the crystal fields Δ_{cef} and Hund's rule coupling J_{Hund} . In the case of a half-filled fully degenerate ($\Delta_{\text{cef}} = 0$) d shell, the moments of valence electrons localized in the d orbitals all coalign, resulting in a large net moment. When $\Delta_{\text{cef}} \simeq J_{\text{Hund}}$, the energy degeneracy of the orbitals is sufficiently lifted. The lowest-energy orbitals can then be filled with electrons having both up and down spins, while the uppermost are empty, and the result is a net reduced moment. By necessity, a high-spin/low-spin transition must be accompanied by a structural modification in which Δ_{cef} is elevated to the order of J_{Hund} .

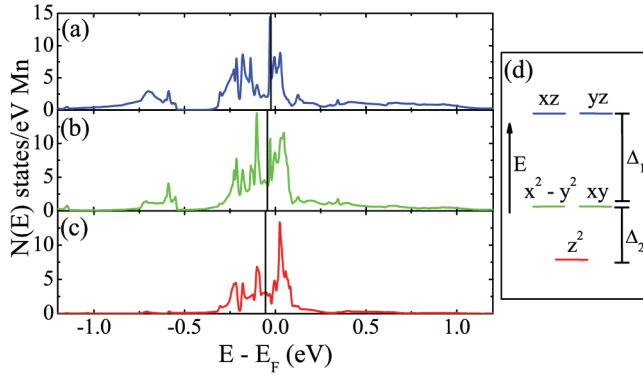


FIG. 10. (Color online) Paramagnetic partial $N(E)$ of the Mn orbitals (a) $3d_{xz+yz}$ (blue curve), (b) $3d_{xy+x^2-y^2}$ (green curve), and (c) $3d_{z^2}$ (red curve). (d) Estimated crystal-field levels and splittings.

To test whether such an explanation is appropriate for CaMn_2Sb_2 , we performed additional electronic-structure calculations above and below $T_N \pm 10$ K, the temperature at which we observed rapid contraction along the c axis. Specifically, we estimated Δ_{cef} using the reported $T = 20$ K lattice parameters and atomic positions determined from neutron diffraction measurements¹⁷ as well as our own structural solution using complete and redundant x-ray data at $T = 110$ K. It is important to note, however, that Δ_{cef} is not a well-defined concept in this material; the Mn atomic states form bands and can not be thought of as truly isolated. Nonetheless, we may estimate this quantity as the difference between the energies at which the quasiparticle peaks associated with each orbital are centered. We evaluate these energies by obtaining the weighted average of the DFT energy eigenvalues ϵ_{ki} as $E_{\text{imp}L} = \sum_{ki} P_k(i, L)\epsilon_{ki}$, where L indexes the orbitals, k the Brillouin zone wave vectors, and i the bands, and P is an operator that projects objects in the band representation into their orbital counterpart.³⁴ In Fig. 10, we show the partial $N(E)$ of the Mn $3d$ orbitals from atomic positions acquired at 110 K. We calculated the paramagnetic $N(E)$ to avoid the interference of spin splitting with the crystal fields. In this state, each group of orbitals is nearly centered about E_F with a quasiparticle width of approximately 0.4 meV. Additional spectral weight is observed out to ± 1.2 eV, particularly in the d_{xz} and d_{yz} orbitals. The results of weighted averaging over both the quasiparticle peak as well as the outlying spectral weight are sketched in the inset, and accordingly we estimate that the xz and yz orbitals are degenerate and separated from the likewise degenerate $x^2 - y^2$ and xy orbitals by $\Delta_1 \sim 20$ meV, while the z^2 orbitals lie deeper in energy by $\Delta_2 \sim 10$ meV. Notably, even the larger of these energy differences is an order of magnitude smaller than the width of the quasiparticle peak. Furthermore, J_{Hund} in related manganese pnictides has been shown to be 0.8 to 0.9 eV.¹⁰ These two points strongly suggest that the crystal-field splitting in CaMn_2Sb_2 is far too weak to explain a crystal-field-induced high-spin/low-spin transition. We therefore suggest that the observed Curie-Weiss-type susceptibility is a product of the weak ferromagnetic state, while the majority of the local Mn moments remain exchanged coupled far into the paramagnetic state, as we have previously observed in the related compound LaMnPO .¹⁰

An important question remains: If IR transmission measurements uncovered direct evidence of states in the gap that should lead eventually to a metallic state, why has an EDT not yet been observed in this system? Perhaps the answer to this question is that the correct dopant has not yet been identified, as was the case for a time with BaMn_2As_2 ,^{9,12} or that further Na doping, if such is possible, may indeed trigger an EDT. Just as likely, however, it may prove necessary to proceed to higher pressures; the limited range of 1.6 GPa undertaken in this study falls short of the ~ 10 GPa required to metallize LaMnPO ,¹⁰ for example. Our extrapolation that antiferromagnetic order could be extinguished by ~ 20 GPa, however, is a testable prediction and indeed suggests that CaMn_2Sb_2 could be driven to a metallic and nonmagnetic ground state.

V. CONCLUSIONS

We have presented a suite of magnetic, transport, optical, and crystallographic measurements as well as electronic-structure calculations in a detailed study of high-quality CaMn_2Sb_2 single crystals. As a result of this study, it has become apparent that undoped CaMn_2Sb_2 is an insulator with a direct optical gap of ~ 1 eV and an activation gap that is significantly smaller, likely the result of E_F pinning by in-gap states that were directly observed in IR transmission measurements. The antiferromagnetic order gives way at $T_N = 85$ K, to be replaced by a ferromagnet with an ordered moment only 0.2% as large that is perhaps generated by the effects of magnetic polarons. We observe an unexpectedly small Curie-Weiss moment that can not be explained by the variety of high-spin/low-spin transition often observed in $3d$ transition-metal systems such as MnAs, suggesting that it results solely from the ferromagnetic state and that the majority of the moments are hidden by strong exchange coupling that dominates even in the paramagnetic state. Doping with Na simultaneously decreases both the resistivity and the IR transmission, but the optical gap remains unchanged, as was observed to be the case in other layered Mn pnictide systems.⁸ On the other hand, La doping results in an anomalous increase of the electrical resistivity as the gap states are eliminated from the IR transmission spectra with the partial collapse of the optical gap. In neither case, however, is T_N significantly reduced, a recurring theme within this family of compounds. We observe a similar trend in high-pressure resistivity measurements, which rapidly quenched the ferromagnetic phase but only resulted in a modest decrease of T_N . These measurements, however, hint that complete destruction of that antiferromagnetic ground state could be achieved with the application of only ~ 20 GPa.

ACKNOWLEDGMENTS

This work was carried out under the auspices of a Department of Defense National Security Science and Engineering Faculty Fellowship via Air Force Office of Scientific Research Grant No. FA 9550-10-1-0191. Use of the National Synchrotron Light Source, Brookhaven National Laboratory, was supported by the U. S. Department of Energy, Office of Science, Office of Basic Energy Sciences, under Contract No. DE-AC02-98CH10886. The authors gratefully acknowledge many useful discussions with K. Haule (Rutgers) on the topic of crystal electric fields and impurity levels.

*jsimonson@bnl.gov

- ¹D. N. Basov, R. D. Averitt, D. van der Marel, M. Dressel, and K. Haule, *Rev. Mod. Phys.* **83**, 471 (2011).
- ²Q. Si and E. Abrahams, *Phys. Rev. Lett.* **101**, 076401 (2008).
- ³K. Haule, J. H. Shim, and G. Kotliar, *Phys. Rev. Lett.* **100**, 226402 (2008).
- ⁴M. Fang, H. Wang, C. Dong, Z. Li, C. Feng, J. Chen, and H. Q. Yuan, *Europhys. Lett.* **94**, 27009 (2011).
- ⁵L. L. Sun, X.-J. Chen, J. Guo, P. Gao, H. Wang, M. Fang, X. Chen, G. Chen, Q. Wu, C. Zhang, D. Gu, X. Dong, K. Yang, A. Li, X. Dai, H.-K. Mao, and Z. Zhao, *Nature (London)* **483**, 67 (2012).
- ⁶J. X. Zhu, R. Yu, H. Wang, L. L. Zhao, M. D. Jones, J. Dai, E. Abrahams, E. Morosan, M. Fang, and Q. Si, *Phys. Rev. Lett.* **104**, 216405 (2010).
- ⁷Z. A. Ren, W. Lu, J. Yang, W. Yi, X. L. Shen, Z. C. Li, G. C. Che, X. L. Dong, L. L. Sun, F. Zhou, and Z. X. Zhao, *Chin. Phys. Lett.* **25**, 2215 (2008).
- ⁸J. W. Simonson, K. Post, C. Marques, G. Smith, O. Khatib, D. N. Basov, and M. C. Aronson, *Phys. Rev. B* **84**, 165129 (2011).
- ⁹A. Pandey, V. K. Anand, and D. C. Johnston, *Phys. Rev. B* **84**, 014405 (2011).
- ¹⁰J. W. Simonson, Z. P. Yin, M. Pezzoli, J. Guo, J. Liu, K. Post, A. Efimenko, N. Hollmann, Z. Hu, H.-J. Lin, C. T. Chen, C. Marques, V. Leyva, G. Smith, J. W. Lynn, L. L. Sun, G. Kotliar, D. N. Basov, L. H. Tjeng, and M. C. Aronson, *Proc. Natl. Acad. Sci. USA* **109**, E1815 (2012).
- ¹¹Y. Sun, J. Bao, C. Feng, Z. Xu, and G. Cao, *Europhys. Lett.* **98**, 17009 (2012).
- ¹²A. Pandey, R. S. Dhaka, J. Lamsal, Y. Lee, V. K. Anand, A. Kreyssig, T. W. Heitmann, R. J. McQueeney, A. I. Goldman, B. N. Harmon, A. Kaminski, and D. C. Johnston, *Phys. Rev. Lett.* **108**, 087005 (2012).
- ¹³J. K. Bao, H. Jiang, Y. L. Sun, W. H. Jiao, C. Y. Shen, H. J. Guo, Z. A. Xu, G. H. Cao, R. Sasaki, T. Tanaka, K. Matsubayashi, and T. Uwatoko, *Phys. Rev. B* **85**, 144523 (2012).
- ¹⁴A. T. Satya, A. Mani, A. Arulraj, N. V. Chandra Shekar, K. Vinod, C. S. Sundar, and A. Bharathi, *Phys. Rev. B* **84**, 180515(R) (2011).
- ¹⁵S. Bobev, J. Merz, A. Lima, V. Fritsch, J. D. Thompson, J. L. Sarrao, M. Gillissen, and R. Dronkowski, *Inorg. Chem.* **45**, 4047 (2006).
- ¹⁶W. Ratcliff II, A. L. Lima Sharma, A. M. Gomes, J. L. Gonzalez, Q. Huang, and J. Singleton, *J. Magn. Magn. Mater.* **321**, 2612 (2009).
- ¹⁷C. A. Bridges, V. V. Krishnamurty, S. Poulton, M. P. Paranthaman, B. C. Sales, C. Myers, and S. Bobev, *J. Magn. Magn. Mater.* **321**, 3653 (2009).
- ¹⁸S. Q. Xia, C. Myers, and S. Bobev, *Eur. J. Inorg. Chem.* **2008**, 4262 (2008).
- ¹⁹K. Momma and F. Izumi, *J. Appl. Crystallogr.* **41**, 653 (2008).
- ²⁰J. Kim and T. Hughbanks, *J. Solid State Chem.* **146**, 217 (1999).
- ²¹P. Blaha, K. Schwarz, G. K. H. Madsen, D. Kvasnicka, and J. Luitz, WIEN2K, An Augmented Plane Wave Plus Local Orbitals Program for Calculating Crystal Properties (Karlheinz Schwarz, Techn. Universität Wien, Austria, 2001).
- ²²J. P. Perdew, K. Burke, and M. Ernzerhof, *Phys. Rev. Lett.* **77**, 3865 (1996).
- ²³J. An, A. S. Sefat, D. J. Singh, and M.-H. Du, *Phys. Rev. B* **79**, 075120 (2009).
- ²⁴Strictly speaking, although the transmission does appear to be higher in the La-doped sample, we can not say absolutely that this increase corresponds to a decrease in conductivity because we do not know the relative thickness of the samples to sufficient accuracy. Rather, this sample could have just been slightly thinner making it appear as though the transmission is slightly greater at lower wave number.
- ²⁵A. Mauger and D. L. Mills, *Phys. Rev. B* **31**, 8024 (1985).
- ²⁶J. M. De Teresa, M. R. Ibarra, P. A. Algarabel, C. Ritter, C. Marquina, J. Blasco, J. García, A. del Moral, and Z. Arnold, *Nature (London)* **386**, 256 (1997).
- ²⁷V. Thampy, J. Kang, J. A. Rodriguez-Rivera, W. Bao, A. T. Savici, J. Hu, T. J. Liu, B. Qian, D. Fobes, Z. Q. Mao, C. B. Fu, W. C. Chen, Q. Ye, R. W. Erwin, T. R. Gentile, Z. Tesanovic, and C. Broholm, *Phys. Rev. Lett.* **108**, 107002 (2012).
- ²⁸Y. Shapira, S. Foner, N. F. Oliveira, and T. B. Reed, *Phys. Rev. B* **10**, 4765 (1974).
- ²⁹S. Takeyama, S. Adachi, Y. Takagi, G. Karczewski, T. Wojtowicz, J. Kossut, and T. Karasawa, *Mater. Sci. Eng. B* **63**, 111 (1999), and references therein.
- ³⁰The lone exception of which we are aware is the ferromagnetic metal MnZnSb; see T. Kanomata, H. Endo, S. Mori, H. Okajima, T. Hihara, K. Sumiyama, T. Kaneko, and K. Suzuki, *J. Magn. Magn. Mater.* **140-144**, 133 (1995).
- ³¹H. Fjellvåg and A. F. Andresen, *J. Magn. Magn. Mater.* **46**, 29 (1984), and references therein.
- ³²N. Menyuk, J. A. Kafalas, K. Dwight, and J. B. Goodenough, *Phys. Rev.* **177**, 942 (1969).
- ³³F. Gronvold, S. Snildal, and E. F. Westrum, *Acta Chem. Scand.* **24**, 285 (1970).
- ³⁴K. Haule, C.-H. Yee, and K. Kim, *Phys. Rev. B* **81**, 195107 (2010).